Discovery of Ordered Tetragonal and Cubic Phases in the Morphotropic Phase Boundary Region of $(1-x)\text{Bi}(\text{Mg}_{3/4}\text{W}_{1/4})\text{O}_3$-$x\text{PbTiO}_3$ Piezoceramics

3.1 Introduction

As discussed in Chapter 1, the crystal structure of the Pb- and Bi-based MPB systems having disordered solid solutions have been investigated extensively [Upadhyay et al. (2015), Pandey et al. (2014)]. However, very less work has been done on the crystal structure analysis of the ordered MPB systems like $(1-x)[Pb(Mg_{0.5}W_{0.5})O_3]-xPbTiO_3$ [Singh et al. (2011)], $(1-x)[Bi(Mg_{3/4}W_{1/4})O_3]-xPbTiO_3$ [$(1-x)BMW-xPT$] etc., that can give an insight about the piezoelectric properties of these materials. In this chapter, we have done in depth structural analysis of the Bi-based solid solution $(1-x)Bi(Mg_{3/4}W_{1/4})O_3-xPbTiO_3$, which is least explored for its crystal structure, phase transition behaviour and structure-property correlations. As discussed in chapter 1, for $(1-x)BMW-xPT$ ceramics, the structure of the morphotropic phase region is reported to be coexisting rhombohedral and tetragonal phases [Snel et al. (2006)]. The structure of the compositions on the lower PT concentration side was reported to be rhombohedral $R3c$ [Snel et al. (2006)]. However, a superlattice peak for B-site cationic ordering is also reported which corresponds to rock-salt structure and is inconsistent with the rhombohedral $R3c$ structure [Stringer et al. (2005)]. Further, no detailed structural analysis has been done across the morphotropic phase boundary for this solid solution. Many ferroelectric perovskite solid solutions having W-ion along with other small cations at B-site are known to exhibit B-site ordered crystal structure [Singh et al. (2011)]. It is therefore imperative to investigate the B-site cationic ordering and correct crystal structure of BMW-PT. The dielectric and phase transition behaviour is also not much explored for BMW-PT solid solution. Lower PT compositions have been reported to have diffused dielectric phase transition while sharp dielectric anomaly is reported for PT rich compositions. There is no study of possible relaxor phase

transition behaviour of various compositions across the MPB. Temperature dependent crystal structure studies have also not been done on this system for investigating the crystallographic phase transitions. Thus a detailed composition and temperature dependent crystal structure and dielectric studies are needed to investigate the structure-property correlations, phase stability regions and nature of phase transitions. Such a study will help us to understand structure-property correlations in other perovskite tungstates like $(1-x)[Pb(Mg_{0.5}W_{0.5})O_3]$-$xPbTiO_3$ exhibiting morphotropic phase boundary and B-site cationic ordering [Singh et al. (2011)].

In this chapter, using Rietveld crystal structure refinement, we have investigated in detail, the crystal structure of BMW-PT across MPB at close compositional interval. Composition and temperature dependent dielectric studies have been performed and correlated with the crystal structure. High temperature XRD measurement has been done to investigate the crystallographic phase transition. Raman and x-ray photoelectron spectroscopic studies have been performed to investigate the local structure and ionization states of W-ions, respectively. Using all these results, we have established a new phase diagram of the BMW-PT ceramic.

3.2 Experimental Procedure

Traditional solid-state ceramic method was used to prepare the $(1-x)[Bi(Mg_{3/4}W_{1/4})O_3]$-$xPbTiO_3$ samples at close compositional interval viz. x = 0.45, 0.50, 0.55, 0.60, 0.61, 0.62, 0.63, 0.64, 0.65, 0.66, 0.67, 0.68, 0.69, 0.70, 0.72, 0.75 and 1.0. Analytical reagent grade Bi_2O_3, MgO, H_2WO_4, TiO_2 and PbO of purity greater than 99% obtained from HiMedia Laboratories Pvt. Ltd. were used as raw materials. Stoichiometric amounts of reactant powders were mixed for 6 hrs in a planetary ball mill (Retsch,

Germany) using acetone as the mixing medium. Dried powder mixture was calcined inside muffle furnace for 6 hrs at an optimized temperature of 850°C. The calcined powders were checked for phase purity using 600W, Rigaku (Japan) Miniflex X-ray diffractometer. The XRD data were collected at a scan rate of 1° min^{-1} in the 2θ range from 10° to 100° at a scan step of 0.02°. The high temperature XRD measurements were done using Rigaku Smart Lab high resolution diffractometer having Johansson CuK$_{\alpha1}$ optics. For making pellets, 2% polyvinyl alcohol (PVA) solution in water was used as the binder. The calcined powder was cold compacted at an optimized load of 70 kN using steel die of 12 mm diameter and uniaxial hydraulic press. The green pellets were kept at 500°C for 12 hrs to remove the binder (PVA) material and then sintered at an optimized temperature of 990°C for 3 hrs. The sintering was carried out in sealed crucible with controlled PbO/Bi$_2$O$_3$ atmosphere using small amounts of PbO and Bi$_2$O$_3$ as sacrificial powder. The density of the sintered pellets was > 97% of the theoretical density. Sintered pellets were crushed into fine powders and annealed at 500°C for 12 hrs before XRD data collection. The microstructure of the sintered pellet surface was studied by scanning electron microscopy (SEM) using a Zeiss Evo Research 18. A thin gold film was sputter-coated on the sintered flat pellets before SEM examination. For dielectric measurements, sintered pellets were electrode by fired on silver paste cured by firing at 500°C for 1h. Dielectric measurements on electroded pellets were carried out using Keysight E4990A Impedance Analyzer. High temperature dielectric measurements were done in heating run at a heating rate of 2°C min^{-1}. The structural analysis by the Rietveld method was carried out using the FullProf Suite [Carvajal (2011)]. The X-ray photoelectron spectra (XPS) were recorded by AMICUS, Kratos, Analytical X-ray photoelectron spectrometer having a monochromatic MgK$_{\alpha}$

(1253.6 eV) source. During data processing of the X-ray photoelectron spectra, binding energy (BE) values were referenced to the C1s peak (284.6 eV). Quantification of the peaks was performed after Shirley background subtraction using XPSPEAK4.1 software. Raman spectra were recorded using STR-300 spectrophotometer with 532 nm laser excitation wavelength and grating 1200 spectrograph with step size of 1.2 cm^{-1}.

3.3 Introduction to the Rietveld Refinement Method

The Rietveld method is extensively recognized and widely accepted for the precise structural analysis of crystalline materials. In recent years this method has been used as a vital tool for quantitative phase analysis in the areas of physics, chemistry, materials science and geology. The Rietveld analysis program was developed by H. M. Rietveld [Rietveld (1967); Rietveld (1969)] to analyze of crystal structure of crystalline materials using neutron, synchrotron or X-ray powder diffraction data [Malmros and Thomas (1977); Khattak and Cox (1977); Young (1993)]. Rietveld method does not predict the crystal structure but it fits an approximated structural model to the experimental data. So, understanding of basic crystal structure is essential for fitting the experimental data. If the starting structural model is correct then true crystal structure can be determined by the refinement. Least squares approach is used to refine the true structure in Rietveld method. In the least square approach theoretical XRD profile is generated using the starting structural model and tried to match with the experimental XRD profile. By adjusting the structural and instrumental parameters in the starting structural model, the difference between theoretical and experimental pattern is minimized to an acceptable level. In the Rietveld method, the quantity used to minimize is χ^2 [Young (1993)]. χ^2 is the weighted

sum of squared differences between the observed $(y_{o,i})$ and calculated $(y_{c,i})$ intensity values at the ith step of the XRD pattern.

$$\chi^2 = \Sigma\ w_i\ (y_{o,i} - y_{c,i})^2 \quad \ldots\ldots\ldots\ldots\ldots\ldots\ (3.1)$$

Where, $w_i = 1/\sigma_{o,i}^2$, $\sigma_{o,i}^2$ is the variance of the observed data $y_{o,i}$ [Young (1993); Prince (2004); David (2004); Toby (2006)]. Various agreement factors are used in Rietveld method to ascertain the quality of fit between experimental and calculated patterns quantitatively. The agreement factor weighted profile R-factor (R_{wp}) which reflect the goodness of fit between experimental and calculated XRD patterns is the square root of the quantity minimised, divided by the weighted intensities [Young (1993); Toby (2006)] defined as

$$R_{wp}^2 = \Sigma\ w_i\ (y_{o,i} - y_{c,i})^2\ /\ \Sigma\ w_i\ (y_{o,i})^2 \ldots\ldots\ldots\ldots\ (3.2)$$

Other agreement factor used in Rietveld fit is expected R-factor (R_{exp}). If N is number of data points, R_{exp} is written as [Young (1993), Toby (2006)]

$$R_{exp}^2 = N/\Sigma w_i\ (y_{o,i})^2 \quad \ldots\ldots\ldots\ldots\ldots\ (3.3)$$

χ^2 can be directly obtained from the expected and weighted profile R-factors

$$\chi^2 = R_{wp}/R_{exp} \ldots\ldots\ldots\ldots\ldots\ldots\ldots\ (3.4)$$

The value of χ^2 should be never less than one. However, if the fit results in $\chi^2 < 1$ which implies that $<(y_{o,i} - y_{c,i})^2>$ is less than $\sigma^2(y_{o,i})$. This may occur due to the fact that standard uncertainties for the data are overestimated or additional parameters have been introduced so that the model is fitting the noise. Such types of features are common in powder diffraction [Toby (2006)]. However, if $\chi^2 \gg 1$, then it may be that the model is logical but the standard uncertainty values are underestimated. Other reason may be that the model is imperfect because there are errors in the data that do not correspond to the

model or finally the model is incorrect [Toby (2006)]. On the other hand, the values of χ^2 nearly equal to 1 does not necessarily means that the fit is correct. This can be achieved by taking different models which can give equivalent fits due to insufficient experimental data [Toby (2006)].

Different types of profile functions have been suggested to define the peak shape of calculated XRD pattern in the Rietveld method. Pseudo-Voigt is one of the widely used functions by crystallographers. Pseudo-Voigt function (pV(x)) is the linear combination of Lorentzian (L(x)) and Gaussian (G(x)) functions which can be written as

$$pV(x)= \eta L(x) + (1- \eta)G(x) \quad \text{.......................} \quad (3.5)$$

The width of the x-ray diffraction peaks (which is also called as full width at half maximum (FWHM)) is a significant parameter during crystal structure analysis. FWHM is a variable parameter and depend upon the diffraction angle 2θ in addition to other instrumental factors. Gaussian component [Cagliotiet al. (1958); Mccusker et al. (1999); Carvajal (2001)] of the FWHM is modeled according to equation (3.6) as

$$FWHM = U\tan^2\theta + V\tan\theta + W \quad \text{..................} \quad (3.6)$$

Where, U, V and W are refinable parameters. Lorentzian component is modeled [Cagliotiet al. (1958); Mccusker et al. (1999); Carvajal (2001)] by equation (3.7).

$$FWHM = X\tan\theta + Y/\cos\theta \quad \text{.....................} \quad (3.7)$$

The values of U, V and W parameters are fixed for the specific diffractometer and nearly constant unless there is no line broadening from the sample due to particle size and/ or strain.

3.4 Details of the Rietveld Refinement of (1-x)BMW-xPT

Rietveld structure refinements were carried out using FULLPROF package [Carvajal (2011)]. The compositions close to the MPB exhibited anisotropic peak broadening similar to Pb-based other MPB ceramics [Singh et al. (2006); Singh et al. (2007)]. The anisotropic peak shape function suggested by Stephens (1999) and also incorporated in the FullProf program was used to refine the structure. In the refinement process the background was modelled using 5th order polynomial while the peak shapes were modeled by Pseudo-Voigt function. Occupancy parameters of all the ions were fixed at the nominal composition during refinement. Zero correction, scale factor, background, half width parameters (U, V and W), lattice parameters, positional coordinates and thermal parameters were varied during the refinement. The isotropic thermal parameter for Pb/Bi ions was very high. In view of this, anisotropic thermal parameters were used for A-site cations (Pb/Bi) for all the compositions except for the cubic compositions with $x \leq 0.60$. The Wyckoff positions and the asymmetric unit for the various space groups used during the Rietveld refinement of structures of BMW-xPT system in the present work are given below:

(i) In the ordered cubic structure with *Fm-3m* space group, the occupancy of Bi/Pb ions were fixed at 1(a) sites (0, 0, 0), Ti/Mg and Ti/W ions at 1(b) sites (1/2, 1/2, 1/2) and oxygen ions at 3(c) sites (1/2, 1/2, 0).

(ii) For the refinement of the cubic structure with space group Fm-3m, we used the cubic unit cell having lattice parameters is $2a_c$ where a_c corresponds to cubic lattice parameter. To fix the origin for the cubic structure, the x, y, z-coordinate of O ion was

fixed at 1/6. In the asymmetric unit of the cubic structure with *Fm*-3*m* space group, Bi/Pb and Ti/Mg or Ti/W ions occupy 3(a) sites at (0, 0, 0) and O ion at the 9(b) site at (x, 2x, z).

(iii) In the tetragonal structure with I4/m space group, the occupancy of Bi/Pb ions were fixed at 1(a) sites (0, 0, z), Ti/Ni and OI in 1(b) sites at (1/2, 1/2, z), and OII in 2(c) sites at (1/2, 0, *z*).

3. 5 Results and Discussion

3.5.1 Crystal Structure Analysis by Rietveld Structure Refinement

Fig. 3.1 shows the powder XRD patterns of $(1-x)Bi(Mg_{3/4}W_{1/4})O_3-xPbTiO_3$ ceramics with x = 0.45, 0.55, 0.50, 0.60, 0.61, 0.62, 0.63, 0.64, 0.65, 0.66, 0.67, 0.68, 0.69, 0.70, 0.72 0.75 and 1.0 sintered at 990°C. As can be seen from this figure, the diffraction profiles of the compositions with lower PT concentrations (x < 0.60) appear as singlet suggesting cubic structure. A very small peak around 19° is seen for x = 0.45 which arises due to ordering of B-site cations, as reported earlier also [Stringer et al. (2005)]. Few barely visible peaks around $2\theta = 27.5$ are also seen in lower PT concentration compositions due to trace amount of impurity Bi_2WO_6 phase [ICDD Card number-39006]. As discussed in Chapter 2, formation of very small impurity phase in BMW-PT ceramics in compositions with low PT concentrations is reported by earlier authors also [Snel et al. (2006)], as the perovskite phase of pure BMW is less stable. This impurity phase disappears for compositions with higher PT concentrations. The XRD patterns of compositions with higher PT concentrations (x > 0.62) show characteristic splitting similar to pure $PbTiO_3$ (x = 1), which suggest that their structure may be tetragonal. The intermediate compositions (x = 0.60, 0.61, 0.62) show mixed nature of splitting in x-ray diffraction profiles (see the peak around 45°) which suggest possibility of phase coexistence in these compositions.

The pseudo-cubic (111) diffraction profile around 39° remains single throughout the composition range investigated, which reveals that the structure should be either cubic or tetragonal for all these compositions.
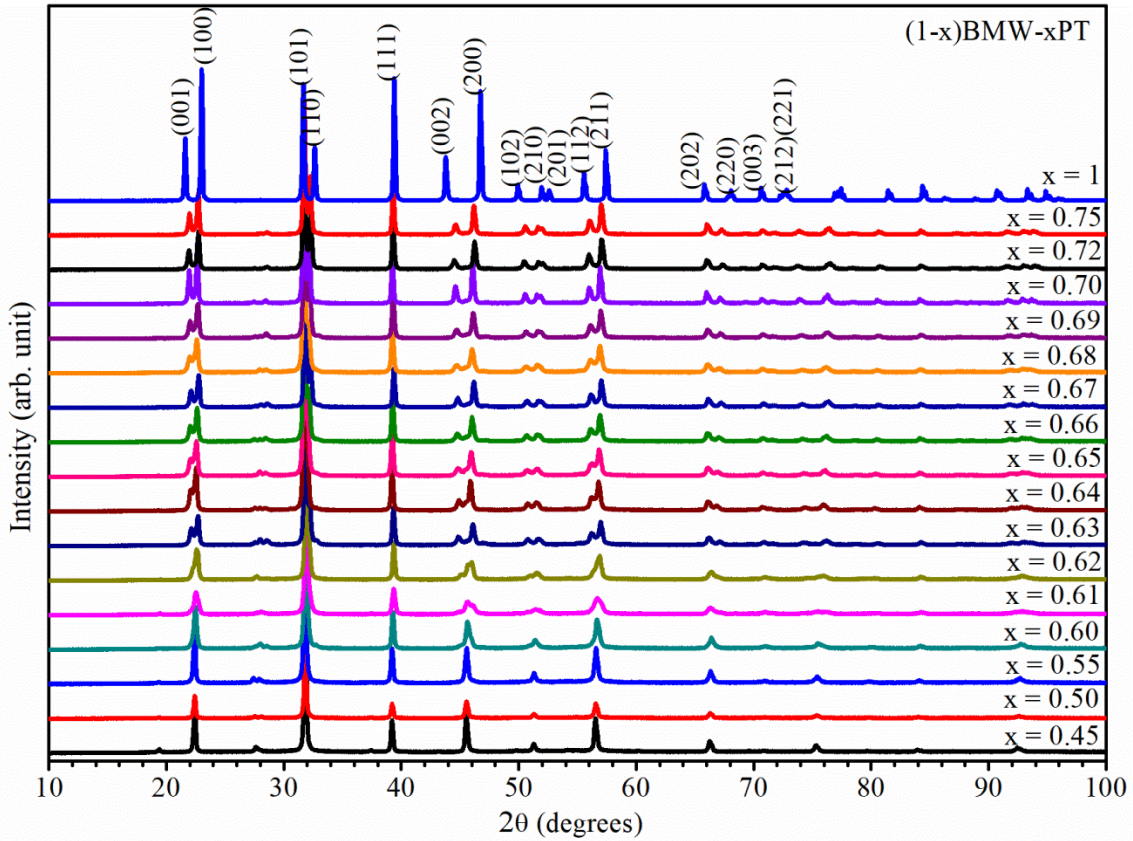

Figure 3.1 Powder XRD patterns of $(1-x)Bi(Mg_{3/4}W_{1/4})O_3-xPbTiO_3$ ceramics with x = 0.45, 0.50, 0.55, 0.60, 0.61, 0.62, 0.63, 0.64, 0.65, 0.66, 0.67, 0.68, 0.69, 0.70, 0.72 0.75 and 1.0 sintered at 990°C. Miller indices using tetragonal structure is given for x = 1.0.

To analyze the room temperature structure of (1-x)BMW-xPT ceramics more precisely, we show in **Fig. 3.2**, the magnified portion of the XRD patterns around 19° and 45° illustrating evolution of superlattice peak due to B-site cation ordering and pseudocubic (200) profiles, respectively.
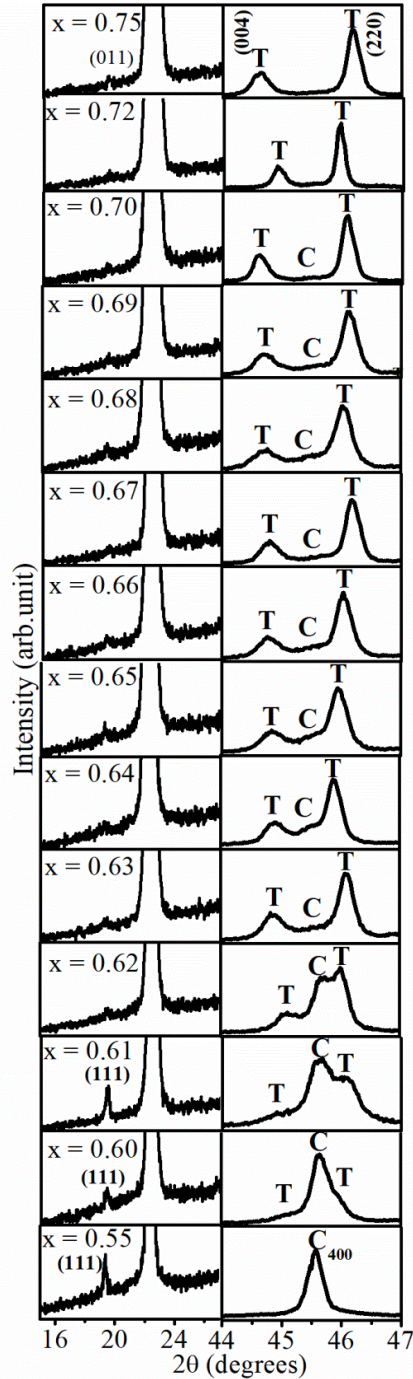
Figure 3.2 Evolution of the selected profiles with composition for $(1-x)Bi(Mg_{3/4}W_{1/4})O_3$-$xPbTiO_3$ ceramics. The superlattice peak (111) indexed using cubic space group (*Fm-3m*) and (011) indexed using tetragonal space group (*I4/m*) arise due to B-site cationic ordering. The peaks marked with "C" and "T" are due to cubic (*Fm-3m*) and tetragonal (*I4/m*) phases respectively.

As can be seen from **Fig. 3.2**, the intensity of superlattice peak is strong enough for the compositions with lower PT concentrations (x < 0.62) and becomes weaker for higher PT concentrations. However, it persist upto x = 0.75 suggesting the presence of B-site cation ordering in all these compositions. With increasing 'x' the intensity of the superlattice reflection at ~19.22° (Miller indices (111) when indexed with respect to doubled pseudocubic cell) appearing due to 1:1 ordering of B-site Mg^{2+}/W^{6+} cations [Snel et al. (2006)] decreases. Thus the increased substitution of Ti^{4+} at Mg^{2+}/W^{6+} sites tends to weaken the cationic ordering in favour of the disordered solid solution. As shown in **Fig. 3.2**, the pseudocubic (200) XRD profile shows singlet character for x = 0.55 suggesting cubic structure. It splits into clear doublet for x = 0.75 corresponding to the tetragonal structure similar to the end member $PbTiO_3$. For the compositions with x = 0.60, 0.61 and 0.62, well resolved triplet is observed in the 200 pseudocubic peak characterizing the coexistence of both the tetragonal and cubic phases corresponding to the structure of the terminal compositions. A weak hump in between the (002), (200) peaks of the tetragonal phase is seen for the compositions with x > 0.62 suggesting presence of small fraction of cubic phase for these compositions as well. The intensity of the (200) peak of the coexisting cubic phase decreases gradually with increasing PT concentration and finally disappears for x = 0.72, suggesting stabilization of pure tetragonal phase for this composition.

To further confirm the crystal structure of various compositions of BMW-PT and to bring out the subtle features of phase coexistence and B-site cationic ordering, we carried out Rietveld structure refinement for all the compositions using x-ray diffraction data. In the Rietveld structure refinement of cubic phase of BMW-PT, we considered that Ti^{4+} ions

are substituting both the Mg^{2+} and W^{6+} sites with doping of PT in BMW. The Ti^{4+} ions were distributed at the Mg^{2+} and W^{6+} sites in the ratio of 3/4:1/4 considering weighted fractions of the Mg^{2+} and W^{6+} ions in the $Bi(Mg_{3/4}W_{1/4})O_3$. Thus, in the asymmetric unit of the cubic *Fm-3m* phase of BMW-PT, the A-site cations Pb^{2+} and Bi^{3+} occupy 8c site at (1/4, 1/4, 1/4) position, the Mg^{2+} occupy 4b sites at (1/2, 1/2, 1/2) position, W^{6+} ions occupy 4a sites at (0, 0, 0) position and O^{2-} ions occupy 24e sites at (1/4+δx, 0, 0) position. The Ti ions were distributed into two parts, 3/4Ti as Ti1 and 1/4Ti as Ti2 occupying Mg^{2+} (4b) and W^{6+} (4a) sites, respectively. As discussed earlier, since the superlattice reflection corresponding to the 1:1 ordering of B-site cations is seen for the tetragonal compositions also, we considered ordered tetragonal structure with I4/m space group in the structure refinement. In the tetragonal phase of BMW-PT with space group I4/m, the A-site cations (Bi^{3+}/Pb^{2+}) occupy 4d sites at (0, 1/2, 1/4), Mg^{2+} ions occupy 2b sites at (0, 0, 1/2), W^{6+} ions occupy 2a sites at (0, 0, 0), O^{2-} (1) ions occupy 4e sites at (0, 0, 1/4+δz) and O^{2-} (2) ions occupy 8h sites at (1/4+δx, 1/4+δy, 0) positions. Similar to the cubic phase, in the Rietveld structure refinement of tetragonal phase also, we considered that Ti^{4+} ions are substituting both the Mg^{2+} and W^{6+} sites. The Ti ions were distributed into two parts 3/4Ti as Ti1 and 1/4Ti as Ti2 occupying Mg^{2+} (2b) and W^{6+} (2a) sites, respectively. For the compositions showing phase coexistence, the occupancies of the ions were taken following same scheme as discussed above for the tetragonal and cubic phases.

Rietveld structure refinement confirms that the structure of BMW-PT with compositions x < 0.60 is B-site ordered cubic phase in the space group *Fm-3m*. For the compositions with 0.60 ≤ x ≤ 0.70, coexistence of ordered tetragonal (*I4/m*) and ordered cubic (*Fm-3m*) structures is seen. The structures of the compositions with characteristic

tetragonal splitting is ordered tetragonal phase in the space group *I4/m*. The Rietveld analysis of XRD data also confirms that BMW-PT ceramics with compositions x > 0.70 exhibit single phase tetragonal structure with space group *I4/m*. Very good fit between observed and calculated profiles obtained for the composition with x = 0.75 using tetragonal (*I4/m*) structure is shown in **Fig. 3.3**(a). **Fig. 3.3**(b) shows the Rietveld fit for the x-ray diffraction pattern of the composition with x = 0.61, considering coexistence of tetragonal (*I4/m*) and cubic (*Fm-3m*) structures. A very good fit between observed and calculated XRD patterns confirms the assigned crystal structures and phase coexistence for this composition. **Fig. 3.3**(c) shows the Rietveld fit for the composition with x = 0.55 considering cubic structure with *Fm-3m* space group. The fit is quite good confirming the *Fm-3m* space group for the BMW-PT compositions with lower PT concentrations. **Table 3.1** lists the refined structural parameters for three representative compositions of the BMW-PT, i.e. cubic, two phase and tetragonal phase regions. Refinement of the coordinates of O(2) ions in tetragonal phase was little unstable and therefore kept to the ideal coordinates. A neutron data will be needed to determine precisely the oxygen positions. The thermal parameters for the A-site cations are very large which suggest large disorder at A-site similar to other Pb-based perovskites [Corker et al. (1998), Dkhil et al. (2001)]. The B-site cationic ordering in BMW-PT results from the large size difference (r_{Mg}^{2+}= 0.89 Å and r_W^{6+} = 0.6 Å) and charge difference between Mg^{2+} and W^{6+} ions. Since the ionic radius and charge of the Ti^{4+} (r_{Ti}^{4+} = 0.74 Å) is in between that of Mg^{2+} and W^{6+} ions, it has no active role in the B-site cationic ordering. This is confirmed by the appearance of disordered solid solution for the BMW-PT compositions with higher PT concentration. Further, as shown in **Fig. 3.2**, the intensity of the superlattice reflection

arising due to 1:1 ordering of B-site cations decreases gradually with increasing PT concentration. This suggests that partial disordered occupancy of B-site cations is also expected for higher PT compositions which finally become fully disordered for the compositions closer to the PT end. A neutron diffraction data will be needed to bring out these subtle features of B-site cation distributions in the tetragonal structure for these compositions.
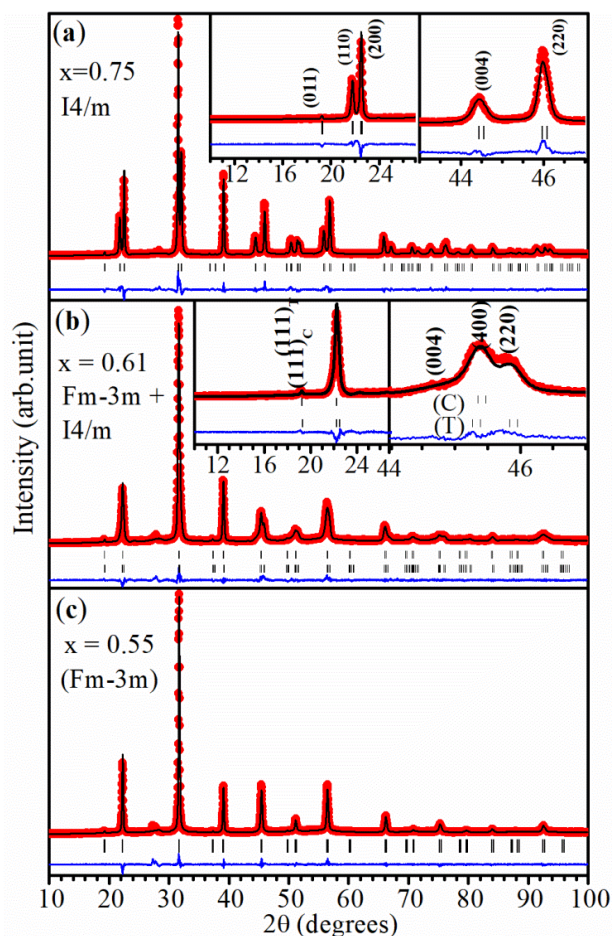

Figure 3.3 Observed (red dots), Rietveld calculated (continuous black line) and their difference (continuous blue curve) profiles for $(1-x)Bi(Mg_{3/4}W_{1/4})O_3-xPbTiO_3$ with (a) x = 0.75 (b) x = 0.61 and (c) x = 0.55 obtained after Rietveld analysis of the powder XRD data using cubic (*Fm-3m*), Cubic + tetragonal (*Fm-3m + I4/m*) and tetragonal (*I4/m*) structures, respectively. The vertical bars above the difference plot show the peak positions. The inset illustrates the goodness of the fit.

70

Table 3.1: Positional coordinates and thermal parameters obtained from structure refinement of (1-x)Bi(Mg$_{3/4}$W$_{1/4}$)O$_3$-xPbTiO$_3$ ceramics with x = 0.55, 0.61 and 0.75 using cubic (*Fm-3m*), coexisting cubic (*Fm-3m*) + Tetragonal (*I4/m*) and tetragonal (*I4/m*) structures respectively. Occupancy of atoms is kept to the nominal values.

Element	X	Y	Z	B	Occupancy
x = 0.55 (*Fm-3m*), χ2 =1.97, R$_{wp}$ = 8.06
Pb	0.250	0.250	0.250	4. 311(7)	0.55
Bi	0.250	0.250	0.250	4. 311(7)	0.45
Mg	0.500	0.500	0.500	0.000	0.3375
W	0.000	0.000	0.000	0.000	0.1125
Ti1	0.500	0.500	0.500	0.000	0.1625
Ti2	0.000	0.000	0.000	0.000	0.3875
O	0.268(2)	0.000	0.000	0.459(2)	3
x = 0.61 (*Fm-3m*), χ2 =1.98, R$_{wp}$ = 9.40
Pb	0.250	0.250	0.250	3.503 (7)	0.61
Bi	0.250	0.250	0.250	3.503 (7)	0.39
Mg	0.500	0.500	0.500	0.00(0)	0.2925
W	0.000	0.000	0.000	0.00(0)	0.0975
Ti1	0.500	0.500	0.500	0.00(0)	0.4575
Ti2	0.000	0.000	0.000	0.00(0)	0.1525
O	0.2332(2)	0.000	0.000	0.00(0)	3
x = 0.61 (*I4/m*), χ2 =1.98, R$_{wp}$ = 9.40
Pb	0.000	0.500	0.250	0.797(2)	0.61
Bi	0.000	0.500	0.250	0.797(2)	0.39
Mg	0.000	0.000	0.500	0.495 (1)	0.2925
W	0.000	0.000	0.000	0.21(3)	0.0975
Ti1	0.000	0.000	0.500	0.190(2)	0.4575
Ti2	0.000	0.000	0.000	0.194(1)	0.1525
O1	0.000	0.000	0.349(7)	0.001 (0)	1
O2	0.250	0.250	0.000	0.329(4)	2
x = 0.75 (*I4/m*), χ2 =1.74, R$_{wp}$ = 7.83
Pb	0.000	0.500	0.250	2.677(4)	0.750
Bi	0.000	0.500	0.250	2.677(4)	0.250
Mg	0.000	0.000	0.500	4.543(4)	0.188
W	0.000	0.000	0.000	0.000	0.062
Ti1	0.000	0.000	0.500	4.543(4)	0.562
Ti2	0.000	0.000	0.000	0.000	0.188
O1	0.000	0.000	0.2132(3)	2.597(5)	1
O2	0.250	0.250	0.000	3.434(3)	2

Fig. 3.4(a) shows the composition dependent variation in the relative phase fractions of the tetragonal and cubic phases across the morphotropic phase coexistence region. Large variation in the phase fractions of the coexisting phases are seen for changing the PT concentration in the compositions range x = 0.60, 0.61 and 0.62. The phase fraction of the cubic phases decreases gradually on the tetragonal phase region side while it changes sharply on the cubic phase region side. Thus the morphotropic phase boundary (MPB) between the stability regions of tetragonal and cubic phases may correspond to the composition around x = 0.61 where one may expect the maximization of the physical properties. This is indeed observed in the composition dependence of room temperature permittivity which is shown in **Fig. 3.4**(b). Room temperature dielectric permittivity measured at 10 kHz frequency on the compositions x = 0.45, 0.50, 0.55, 0.60, 0.61, 0.62, 0.63, 0.64, 0.65, 0.66, 0.67, 0.68, 0.69, 0.70, 0.72, 0.75 and 1.0 is shown in **Fig. 3.4**(b). As can be seen from **Fig. 3.4**(b), the dielectric permittivity is less than 400 for the compositions away from the MPB region. The permittivity value increases three times (~1250) and shows a peak around x = 0.61 corresponding to the MPB. The value of the permittivity is higher in the phase coexistence region and decreases fast in the single phase region. Even though both the ordered tetragonal and cubic phases in the MPB region are Centro-symmetric, forbidding any ferroelectric activity, the structural instability at the morphotropic phase transition is attributed to the enhanced dielectric response at the morphotropic phase boundary. Relaxor behaviour is also expected to enhance the dielectric response for these compositions.
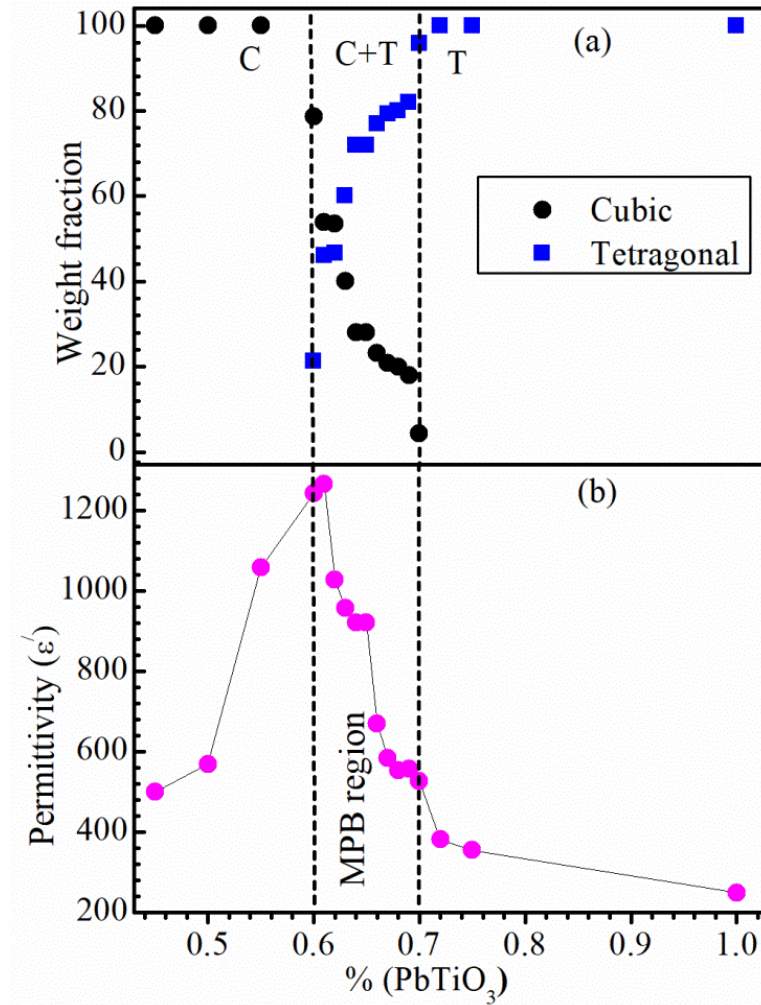
Figure 3.4 Composition dependence of (a) cubic and tetragonal phase fractions and (b) permittivity at room temperature for $(1-x)Bi(Mg_{3/4}W_{1/4})O_3-xPbTiO_3$ ceramics.

Fig. 3.5(a) shows the variation of lattice parameters with composition across the MPB for BMW-PT ceramics. For easy comparison of the lattice parameters of cubic (*Fm-3m*) phase compositions with the tetragonal (*I4/m*) phase compositions, the lattice parameters of the two structures are suitably scaled. The refined values of lattice parameters for various compositions of BMW-PT across MPB are listed in **Table 3.2**. In the single phase cubic region (x < 0.60) the lattice parameter shows slightly decreasing trend with increasing PT

concentration. The ionic radii of Mg^{2+} and W^{6+} are 0.89 Å and 0.6 Å respectively. The effective ionic radii of B-site cations with Mg^{2+}/W^{6+} occupancy will be ~0.8175 Å. Substitution of Mg^{2+}/W^{6+} cations by Ti^{4+} ions (ionic radii ~0.74 Å) will decrease the effective ionic radius of B-site cations, there by introducing small decreasing trend in the unit cell volume and cubic lattice parameter, with increasing PT concentration. In contrast, the substitution of A-site Bi^{3+} ions (ionic radius = 1.17 Å) by bigger Pb^{2+} ions (ionic radius = 1.49 Å) should increase the lattice parameter for compositions with higher PT concentrations. However, as shown in **Fig. 3.5**(b) the unit cell volume has a decreasing trend with increasing PT concentration. This suggests that A-site cationic substitution does not have active role on the structural distortion, possibly due to local A-site disorder which is well known in Pb-based perovskites [Corker et al. (1998), Dkhil et al. (2001)]. This is indeed confirmed by the bond lengths given in **Table 3.3** for three representative compositions. The A-O bond length is nearly unchanged with changing compositions. For the tetragonal phase, as shown in **Fig. 3.5**(a), the c- parameters increases while a-parameter decreases with increasing PT concentration for the compositions with x > 0.61. Increasing PT concentration is expected to increase the tetragonality (c/a) and difference in the 'c' and 'a' parameters of the tetragonal phase. **Fig. 3.5**(b) shows the composition dependence of unit cell volume for majority phase and tetragonality (c/a) for $(1-x)Bi(Mg_{1/2}W_{1/2})O_3$-$xPbTiO_3$ ceramics. As expected, tetragonality increases with increasing PT concentration. The unit cell volume decreases continuously with increasing PT concentration for both the cubic and tetragonal structures. This is attributed to the substitution of Mg^{2+}/W^{6+} cations by smaller Ti^{4+} ions at B-site. Reduction in the unit cell volume with increasing PT concentration further confirms that the A-site cationic substitution of smaller Bi^{3+} with

larger Pb^{2+} does not have active role on the structural distortion, because of locally disordered A-sites.
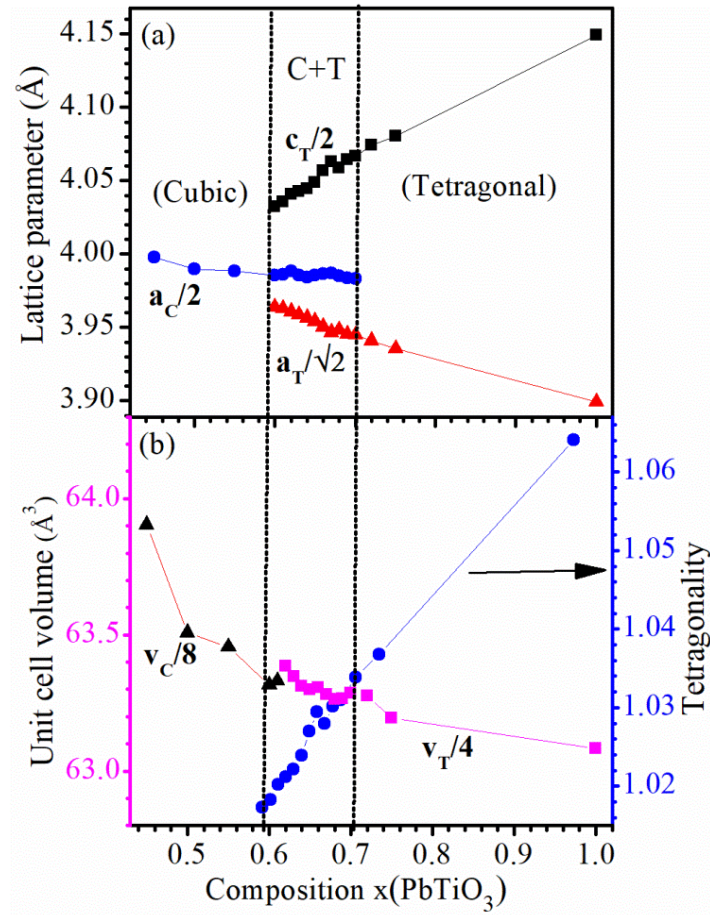

Figure 3.5 Composition dependence of (a) lattice parameters (b) unit cell volume and tetragonality for $(1-x)Bi(Mg_{3/4}W_{1/4})O_3-xPbTiO_3$ ceramics.

Table 3.2: Refined Lattice parameters of $(1-x)Bi(Mg_{3/4}W_{1/4})O_3$-$xPbTiO_3$ ceramics for the composition range $0.45 \leq x \leq 1.0$.

(1-x)BMW-xPT Compositions (x)	Lattice parameters		χ^2	R_{wp}
	a (Å)	c (Å)		
0.45	a_C =7.996(3)	…………	2.17	8.66
0.50	a_C =7.97942(4)	…….........	1.60	11.10
0.55	a_C =7.97723(3)	…………	1.97	8.06
0.60	a_C =7.9714(4) a_T =5.60555(7)	c_T =8.06461(1)	3.72	11.50
0.61	a_C =7.97205(7) a_T =5.60435(7)	c_T =8.07065(1)	1.98	9.10
0.62	a_C =7.97427(8) a_T =5.58440(4)	c_T =8.11818(1)	2.95	10.60
0.63	a_C =7.9701(9) a_T =5.58771(3)	c_T =8.10814(1)	2.93	10.80
0.64	a_C =7.96825(9) a_T =5.5954(2)	c_T =8.08864(5)	3.08	9.81
0.65	a_C =7.97116(7) a_T =5.59192(3)	c_T =8.0971(6)	3.10	10.01
0.66	a_C =7.97322(2) a_T =5.58654(3)	c_T =8.1138 (5)	3.49	11.00
0.67	a_C =7.97415(3) a_T =5.58133(3)	c_T =8.12567(5)	3.99	12.40
0.68	a_C =7.96975(7) a_T =5.58344(3)	c_T =8.11709(6)	3.47	10.06
0.69	a_C =7.96777(3) a_T =5.57962(3)	c_T =8.12862(2)	3.90	11.70
0.70	a_C =7.96668(2) a_T =5.57878(3)	c_T =8.1337(2)	2.87	11.07
0.72	a_T =5.57317(2)	c_T =8.14862(3)	2.34	9.34
0.75	a_T =5.56558(2)	c_T =8.16064(4)	1.74	7.83
1	a_T =3.89922(3)	c_T =4.14915(6)	1.60	8.07

Coexistence of the cubic and tetragonal phases in the W-based perovskite solid solutions has been reported in other MPB ceramics also such as $(1-x)Pb(Mg_{1/2}W_{1/2})O_3$-$xPbTiO_3$ [Singh et al. (2011)], $(1-x)Pb (Fe_{2/3}W_{1/3})O_3$-$xPbTiO_3$ [Mitoseriua et al. (2002)] and the Phase coexistence region in these ceramics is also very wide. The wide compositional width of the phase coexistence region in the MPB ceramics is reported to be linked with the tolerance factor differences of the two components of the solid solution. Suchomel and Davies [Suchomel et al. (2004)] have reported that larger difference in the tolerance factor of the two components of the solid solution leads to narrow phase coexistence region in the MPB system and MPB appears at larger PT concentration. The tolerance factor for BMW is 0.884 while it is 1.027 for PT which suggests that MPB is expected for this system at higher PT concentration. However, the larger phase coexistence region in BMW-PT might be appearing due to B-site cationic ordering of the two components. In another MPB system $(1-x)Bi(Mg_{1/2}Zr_{1/2})O_3$-$xPbTiO_3$, the tolerance factor for $Bi(Mg_{1/2}Zr_{1/2})O_3$ is 0.9257 which differs reasonably with that for the PT (1.027). This system shows narrow compositional with of the phase coexistence region and MPB also appears at larger PT concentration (x = 0.56) [Pandey et al. (2014)]. This system obeys exactly the predictions of the Suchomel and Davies [Suchomel et al. (2004)] which suggest that the large difference in the tolerance factor in the end components of the MPB system results in the narrow phase coexistence region across the MPB.

Table 3.3: Selected bond lengths (Å) and bond angles (degree) extracted from the refined structures of $(1-x)Bi(Mg_{3/4}W_{1/4})O_3-xPbTiO_3$ Ceramics.

Type of bonds	x = 0.55 (Cubic)	x = 0.61 (Cubic)	Type of bonds	x = 0.61 (Tetragonal)	x = 0.75 (Tetragonal)
Bi-O (Å)	2.8205(5)	2.8211(7)	Pb/Bi-O(1) (Å)	2.907(2)	2.803(3)
Pb-O (Å)	2.8205(5)	2.8211(7)	Pb/Bi-O(2) (Å)	2.8279(2)	2.83417(5)
Mg/Ti1-O (Å)	1.96(4)	2.113(16)	Mg/Ti1-O(1) (Å)	2.79(6)	2.34(3)
			Mg/Ti1-O(2) (Å)	1.9814(2)	1.97041(5)
W/Ti2-O (Å)	2.03(4)	1.873(16)	W/Ti2-O(1) (Å)	1.24(6)	1.74(3)
			W/Ti2-O(2) (Å)	1.9814(2)	1.97041(5)
Pb/Bi-O-Pb/Bi	89.99(2)	89.90(3)	Pb/Bi-O(1)-Pb/Bi	85.90(6)	89.4(1)
			Pb/Bi-O(2)-Pb/Bi	88.961(8)	91.908(2)

Fig. 3.6 shows the schematic unit cells for ordered cubic (*Fm-3m*) ordered tetragonal (*I4/m*) and disordered tetragonal (*P4mm*) structures. The ordering of the B-site cations leads to non-primitive larger unit cells while the disordered structure corresponds to the primitive perovskite cell.
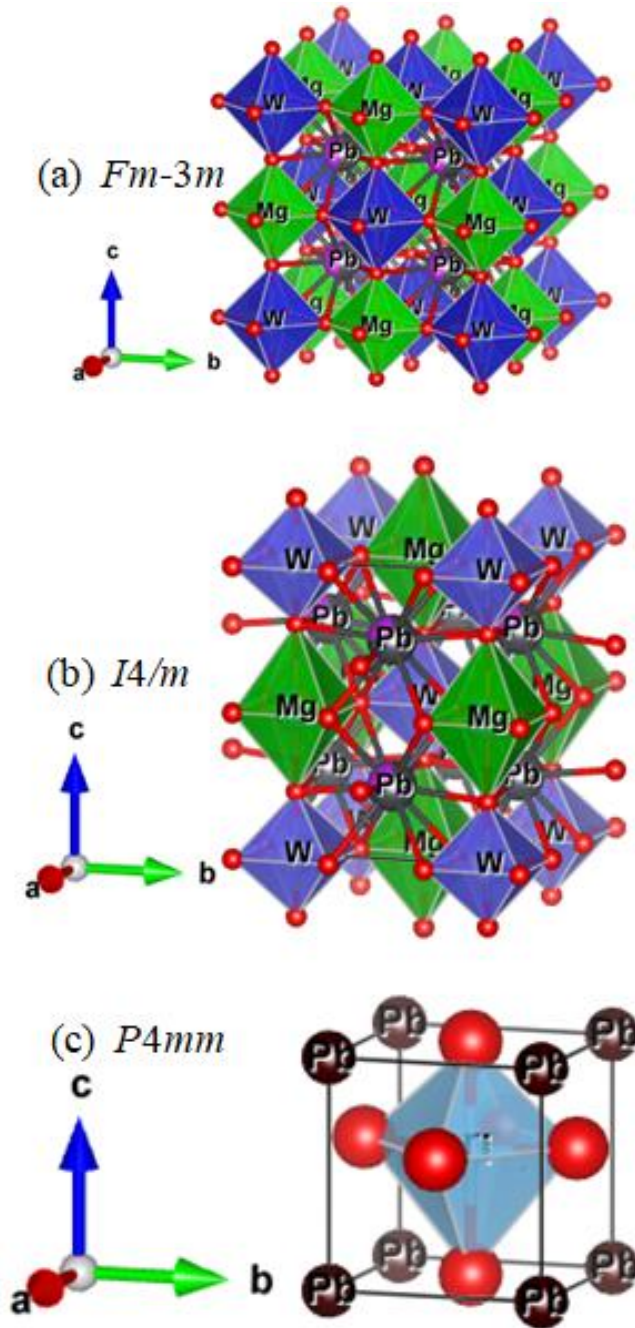
Figure 3.6 Schematic unit Cells for (a) Cubic (*Fm*-3*m*), (b) Tetragonal (*I4/m*) and (c) Tetragonal (*P4mm*) phases of (1-x)Bi(Mg$_{3/4}$W$_{1/4}$)O$_3$-xPbTiO$_3$ ceramics.

3.5.2 Raman Studies

According to factor group analysis nine Raman active modes represented as M = $3A_g + 3B_g + 3E_g$ should be observed for tetragonal structure with *I4/m* space group. In case of the ordered cubic phase with space group *Fm-3m*, 4 Raman active modes A_{1g}, E_g and $2T_{2g}$ (F_{2g}) are expected. The A_{1g} and two fold degenerate E_g modes correspond to stretching of BO_6 octahedra. The F_{2g} modes are three fold degenerate, one of them corresponds to the O-B-O bending of the octahedra and the other one is linked with the A-site cation translations [Manoun et al. (2010), Manoun et al. (2012), Andrews et al. (2015)]. In single component double perovskite tungstates, the A_{1g} and T_{2g} modes are usually very strong and the E_g mode is comparatively weak [Manoun et al. (2010), Manoun et al. (2012), Andrews et al. (2015)]. However, in solid solutions systems, the Raman intensity of these modes may not differ much. **Fig. 3.7**(a) shows the Raman spectra of $(1-x)Bi(Mg_{3/4}W_{1/4})O_3$-$xPbTiO_3$ ceramics with compositions x = 0.55, 0.62, 0.66 and 0.75, respectively. For comparison, we have shown in **Fig. 3.7**(b), the Raman spectra for the pure $PbTiO_3$ also, which is tetragonal with *P4mm* space group and no B-site cationic ordering is present [Burns et al. (1973)]. Position of various Raman mode peaks corresponding to different structures and space groups are marked in **Fig. 3.7**. Raman modes for *Fm-3m* space group are marked in bottom curve of **Fig. 3.7**(a) while top curve is marked for the position of Raman modes for *I4/m* space group. As reported in several other double perovskites, B-site cationic ordering results in strong Raman active peaks near ~ 875 cm^{-1} and 50 cm^{-1} [Waeselmann et al. (2013)]. As can be seen from **Fig. 3.7**, a strong peak is observed around 875 cm^{-1} for BMW-PT with x = 0.55, 0.62, 0.66 and 0.75 confirming the B-site cationic ordering and double perovskite structure for all these compositions. Due to experimental

limitation, we could not record the second Raman mode peak expected around 50 cm^{-1} corresponding to the B-site cationic ordering. The peak around 875 cm^{-1} is absent in the Raman spectrum of pure PbTiO$_3$ which has primitive perovskite structure without any B-site cationic ordering [Burns et al. (1973)].
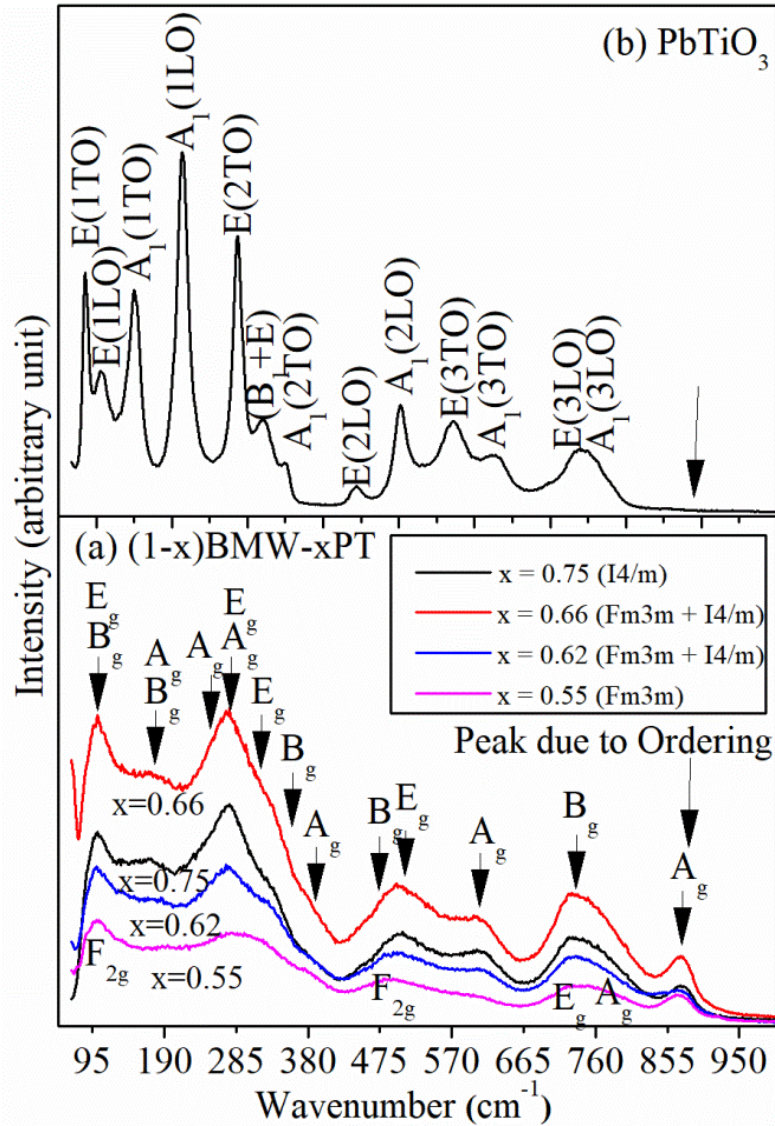

Figure 3.7 Raman spectra of (a) (1-x)Bi(Mg$_{3/4}$W$_{1/4}$)O$_3$-xPbTiO$_3$ with x = 0.55, 0.62, 0.66, 0.75 and (b) pure PbTiO$_3$.

Thus our results of Rietveld structural analysis for the presence of *Fm-3m* and *I4/m* space groups for the cubic and tetragonal structures in the compositions across the MPB region of BMW-PT is confirmed by the Raman spectroscopic analysis. As revealed by our Rietveld structural analysis, the compositions with x = 0.62 and 0.66 have coexisting tetragonal and cubic phases while x = 0.55 is pure cubic (*Fm-3m*) and x = 0.75 is pure tetragonal (*I4/m*). However, the Raman spectrum shown in **Fig. 3.7**(a) suggests that observed Raman lines for all these four compositions are nearly similar. This suggests that even the cubic (x = 0.55) composition have some local regions with tetragonal distortions which are not appearing in the average structure investigated by powder XRD characterization. Local structure differing from the average structure determined from powder XRD is well known in many Pb-based perovskite solid solutions [Corler et al. (1998), Dkhil et al. (2001)]. In relaxor ferroelectrics like $Pb(Mg_{1/3}Nb_{2/3})O_3$, $Pb(Zn_{1/3}Nb_{2/3})O_3$ and $Pb(Fe_{0.5}Nb_{0.5})O_3$, the average structure as determined from powder diffraction is reported to be cubic while local structure is known to be rhombohedrally distorted [Bokov et al. (2006)]. As can be seen from **Fig. 3.7**(a), the intensity of the Raman peaks corresponding to the tetragonal *I4/m* structure decreases and gets broadened with decreasing the PT concentration. This confirms that the tetragonal structure is gradually destabilizing in favor of cubic $Fm\text{-}3_m$ phase with decreasing the PT concentration of the solid solution near MPB.

3.5.3 X-ray Photoelectron Spectroscopic (XPS) Characterization

Fig. 3.8 shows the x-ray photoelectron spectra (solid circle dots) of W4f ad O1s core levels of the (1-x)BMW-xPT for the compositions with x = 0.64 and 0.75. Two well resolved peaks with asymmetric tails are seen for the XPS of W4f whereas only one clear

peak with asymmetric tails is seen for the O1s. In **Fig. 3.8**, the continuous line overlapping the observed XPS data (solid circle dots) corresponds to the resulting curve fit, while the bottom curve (stars) shows fitted Shirley background. As reported in the case of other tungstate compounds by earlier authors [Rahimnejad et al. (2014), Kalhori et al. (2016)], the good fit for the XPS of tungsten (W4f) required using core level peak for both the W^{+6} and W^{+5} ionization states. De-convolution of the XPS of tungsten suggests that binding energy peaks for both the W^{6+} and W^{5+} ions are present. After fitting, the positions of the core level peaks for W^{6+} are obtained as $4f_{7/2}$ at ~38.8 eV (solid triangles) & $4f_{5/2}$ at 36.2 eV (solid squares) and for W^{5+} ion $4f_{7/2}$ at ~37.64 eV (solid triangles) & $4f_{5/2}$ at 35.36 eV (solid squares), for the composition with x = 0.64 shown in **Fig. 3.8**(a). As shown in **Fig. 3.8**(b), for the composition with x = 0.75 also, we needed 4 peaks corresponding to the W^{6+}, $4f_{7/2}$ at ~38.64 eV (hallow triangles) & $4f_{5/2}$ at 36.37 eV (hallow squares) and for W^{5+} ion, $4f_{7/2}$ at ~37.16 eV (hallow triangles) & $4f_{5/2}$ at 35.51 eV (hallow squares). The areas under peaks corresponding to the XPS transitions in W^{+6} and W^{+5} were used to calculate the relative proportions of these ions in both the samples. We find the greater proportion of the W^{+6} ions and smaller proportion of the W^{5+} ions by XPS analysis. Since the XPS spectra of O1s also exhibits broad asymmetric peak, to obtain a good fit, we needed to use four peaks for the composition with x = 0.64 as shown in **Fig. 3.8**(c). After fitting, the obtained four peaks for the O1s at ~531.13 eV (solid triangles) corresponds to the transitions for lattice oxygen, ~532.27 eV (solid squares) for oxygen vacancy, ~533.63 eV (hallow triangles) for surface oxygen and 535.86 eV for water vapour oxygen (hallow circles). The small peak for the water vapour oxygen might be arising because of water vapour absorbed from the atmosphere due to hygroscopic nature of the sample. In

contrasts, the fitting of the XPS spectra of O1s for the composition with x = 0.75 [see **Fig. 3.8**(d)] required three peaks only that correspond to the transitions for lattice oxygen at ~530.80 eV (solid triangles), for oxygen vacancy at ~531.84 eV (solid squares) and for surface oxygen at ~533.12 eV (hallow circles). Above results suggests that significant oxygen vacancies are present in the samples and lower PT concentrations are little bit hygroscopic in nature. Presence of oxygen vacancies are expected to promote the formation of W^{5+} ions to maintain the charge neutrality which is indeed observed from the XPS characterization of the tungsten ions in the sample.
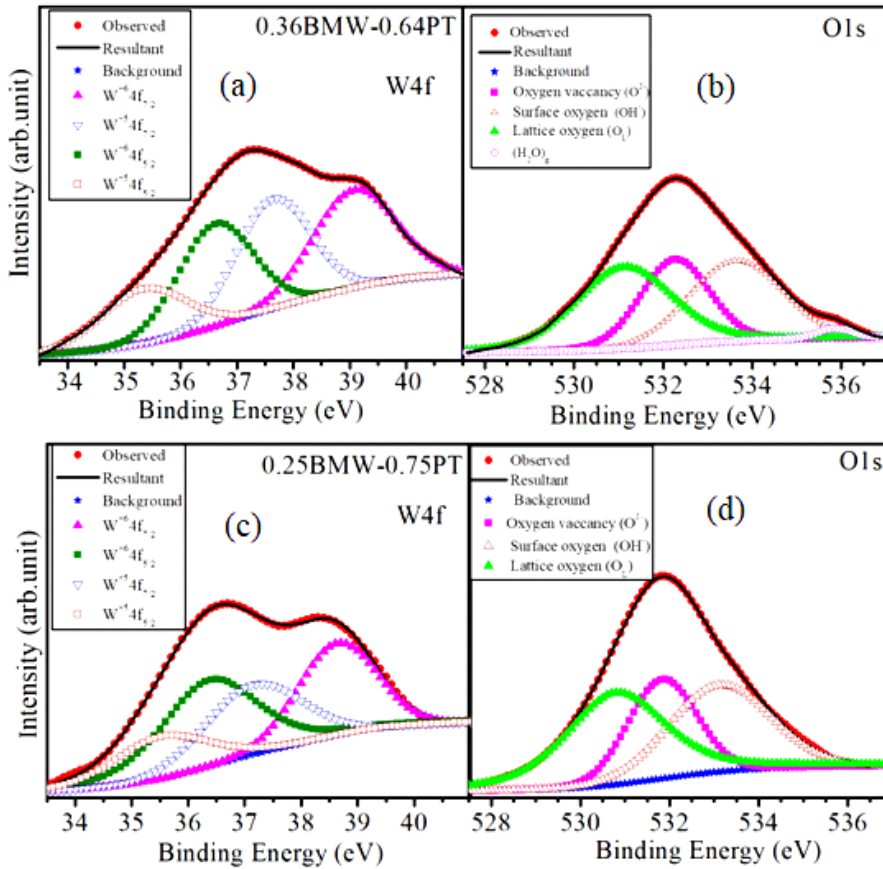
Figure 3.8 X-ray photoelectron spectra (XPS) of W4f and O1s core levels for (1-x)Bi(Mg$_{3/4}$W$_{1/4}$)O$_3$-xPbTiO$_3$ ceramics with x = 0.64 and 0.75. Symbols for curves obtained after deconvolution of various contributions and peak fittings, are specified in the insets.

3.5.4 High Temperature Dielectric Studies

Temperature dependence of dielectric permittivity ($\varepsilon^/$) and loss tangent (tan δ) at various frequencies in the range 100kHz-2MHz for six representative compositions of (1-x)BMW-xPT ceramics is shown in **Fig. 3.9**. We have selected two compositions each from the cubic (x = 0.45, 0.55), two phase (x = 0.61, 0.64) and tetragonal (x = 0.72, 0.75) phase regions to investigate subtle features of dielectric phase transitions in (1-x)BMW-xPT ceramics.

As can be seen from **Fig. 3.9**, the temperature dependence of the dielectric permittivity ($\varepsilon^/$) exhibits two peaks for all these compositions. The two dielectric peaks are coming closer to each other with increasing PT concentrations. The peak on the higher temperature side appears nearly at the same temperature (~450°C) for all the compositions and become stronger with increasing PT concentration. This suggests that the origin of this peak is not linked with the original crystal structure of the samples at room temperature. This peak is attributed to originate from the dielectric relaxation linked order disorder transition of the multiple charge states of B-site cations ($Mg^{2+}/W^{6+}/W^{5+}/Ti^{4+}$). Creation of the oxygen vacancies also results in the formation of W^{6+}/W^{5+} mixed ionization states. Appearance of strong dielectric anomaly at charge ordering transition is well known in many rare earth charge ordered perovskite manganites [Mercone et al. (2004)]. It is likely that this dielectric anomaly on the higher temperature side is resulting from the transformation of the some fraction of the ordered phase of BMW-PT into disordered cubic phase. Since ordered cubic phase (*Fm-3m*) is also present with the disordered cubic phase (*Pm-3m*) it will be difficult to distinguish the two phases and their relative proportions by XRD studies. This observation is further confirmed by the enhancement of the second

dielectric anomaly on the higher temperature side in various compositions with increasing PT concentrations as the increased fraction of PT is expected to promote the formation of disordered phase. At higher PT concentrations, the ordered tetragonal phase will gradually transform into the disordered tetragonal phase (space group *P4mm*). Consequent upon this ordered to disordered tetragonal phase transition, the first dielectric anomaly will eventually merge to the second dielectric anomaly and will correspond to the phase transition from disordered tetragonal phase (*P4mm*) to disordered cubic phase (*Pm-3m*). In well studied relaxor $Pb(Sc_{0.5}Ta_{0.5})O_3$ having B-site cationic ordering, it is reported that the degree of ordering of the B-site cations has strong influence on the nature of phase transition [Chu et al. (1993)]. The sample with disordered B-site cations exhibit diffuse phase transition while normal first order ferroelectric phase transition is observed in the samples with well ordered B site (Sc^{3+}/Ta^{5+}) cations [Chu et al. (1993)].
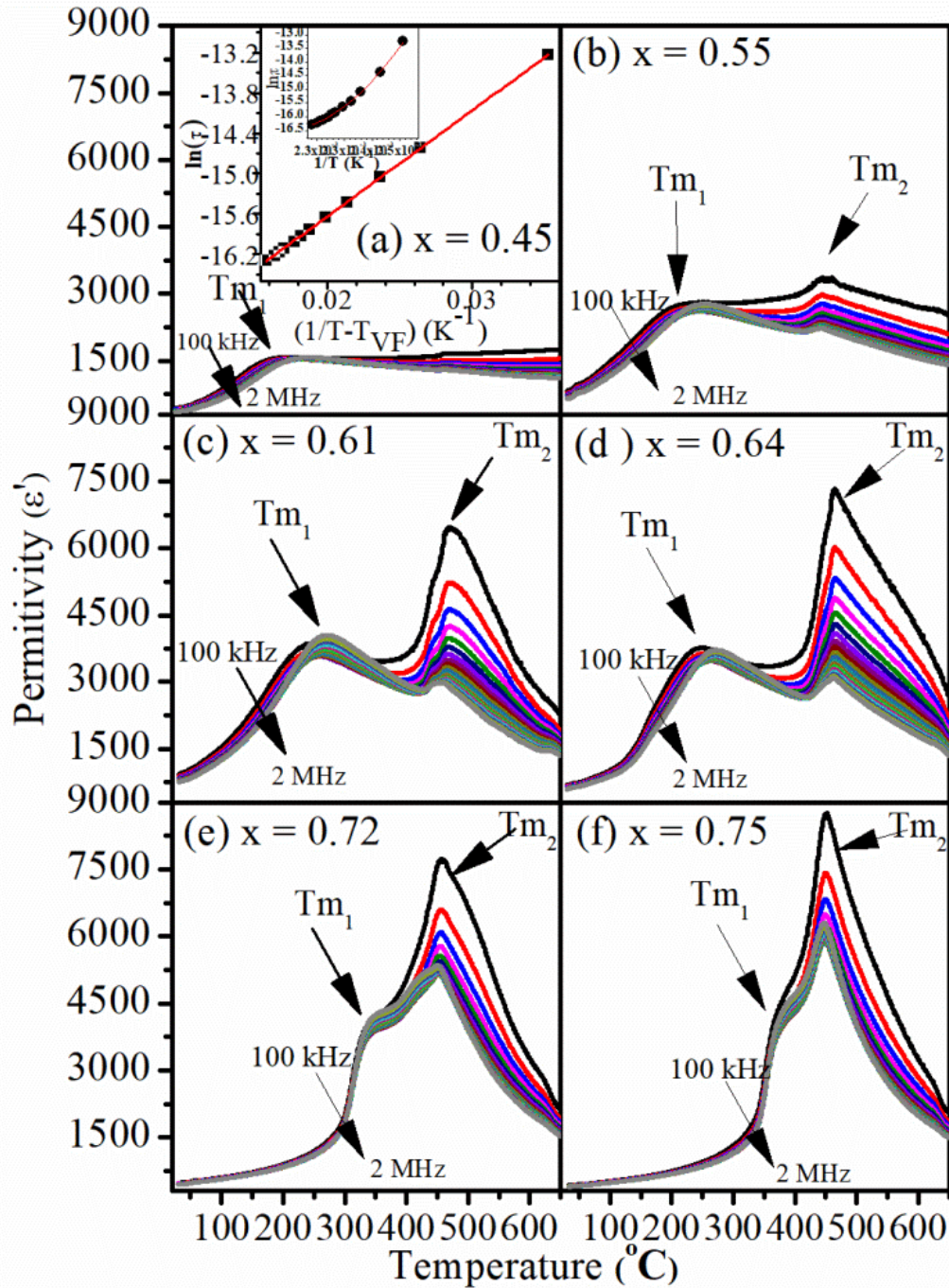
Figure 3.9 Temperatue dependence of the real (ε') part of the permittivity for various compositions of $(1\text{-}x)Bi(Mg_{3/4}W_{1/4})O_3\text{-}xPbTiO_3$ ceramics (a) x = 0.45, (b) 0.55, (c) 0.61, (d) 0.64, (e) 0.72 and (f) 0.75 measured in the frequencie range from 100 KHz to 2 MHz. Inset of (a) shows the Arrehenius and Vogel-Fulcher fits for the relaxation time at various frequencies.

As can be seen from **Fig. 3.9**, the dielectric peak on the lower temperature side continuously shifts on the higher temperature side with increasing PT concentration of the compositions. It is well known in many other ferroelectric solid solutions that increasing PT concentration increases the relaxor and ferroelectric phase transition temperatures [Bokov et al. (2006), Singh et al. (2006)]. Thus the dielectric peak on the lower temperature side must be originating due to structural phase transition from tetragonal/two-phase compositions to cubic phase. As shown in the subsequent section the first peak in the dielectric permittivity in tetragonal compositions corresponds to tetragonal (*I4/m*) to cubic (*Fm-3m*) structural phase transition. In cubic compositions (x = 0.45, 0.55) this dielectric anomaly is due to relaxor transitions. It is evident from **Fig. 3.9** and **Fig. 3.10** that, both the dielectric permittivity ($\varepsilon^/$) and dielectric loss peaks appearing on the lower temperature side exhibit significant frequency dispersion. The peaks in first dielectric anomaly shift to higher temperature side with increasing measuring frequency. Further, the peak in temperature dependence of tanδ appears at lower temperatures than the peak in the real part of the dielectric permittivity ($\varepsilon^/$) for all the compositions. These features indicate relaxor nature of phase transition for the dielectric anomaly appearing on the lower temperature side.
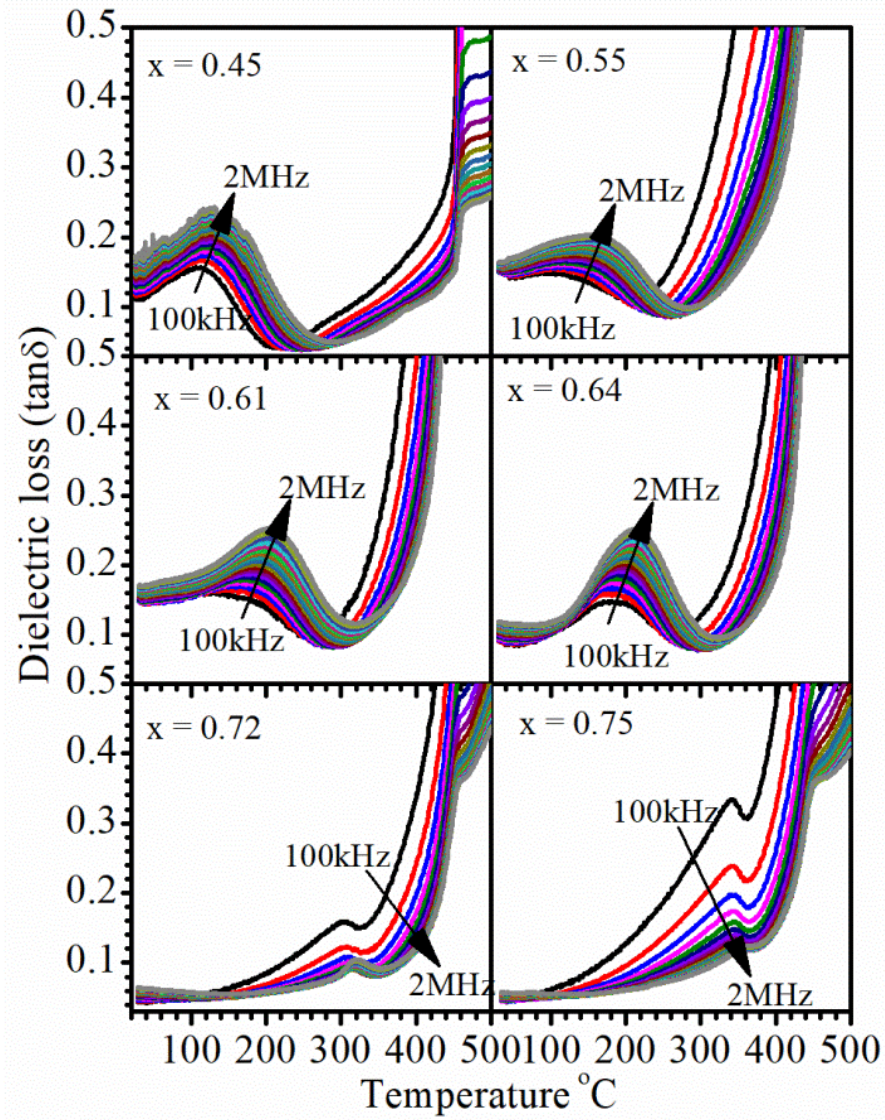
Figure 3.10 Temperatue dependence of the dielectric loss (tan δ) for various compositions of $(1-x)Bi(Mg_{3/4}W_{1/4})O_3$-$xPbTiO_3$ ceramics measured in the frequencie range 100 KHz to 2 MHz.

To verify it further, we show in **Fig. 3.11**, the real and imaginary parts of the permittivity at 100 kHz for the six compositions which also corroborate that the peak/anomaly in the imaginary part of the permittivity appears at lower temperatures than that in the real part. This clearly confirms that the dielectric anomaly peaks on the lower

temperature side in the temperature dependence of permittivity exhibit relaxor nature of the phase transition for all the investigated compositions. **Fig. 3.12** shows the composition dependence of the peak/anomaly temperatures in the real ($T_m^{/}$) and imaginary parts ($T_m^{//}$) of the permittivity and their difference [$T_m^{/}$-$T_m^{//}$], measured at 100 kHz for various compositions of BMW-PT. As can be seen from this figure, the lower PT concentration compositions have large difference in $T_m^{/}$ and $T_m^{//}$ which gradually decreases with increasing PT concentration. This suggests that relaxor nature of phase transition will gradually convert to normal ferroelectric phase transition at higher PT compositions. It is also obvious from the sharper permittivity peaks for the compositions with higher PT concentrations as shown in **Fig. 3.9**. To understand the nature of relaxor phase transition, we modelled the relaxation time (τ) by Arrhenius and Vogel-Fulcher type relations [Pandey et al. (2014)]. The inset to **Fig. 3.9**(a) for the composition with x = 0.45 shows the Arrhenius and Vogel-Fulcher type fits for the relaxation time (τ). A can be seen in this figure, the Arrhenius fit is nonlinear while the Vogel-Fulcher relation gives quite satisfactory linear fit. The obtained activation energy (E_a) is 13.42 meV and the Vogel-Fulcher freezing temperature is 104.35°C (377.35 K) where the relaxor state transforms into a nonergodic relaxor state due to freezing of polar nano-regions.
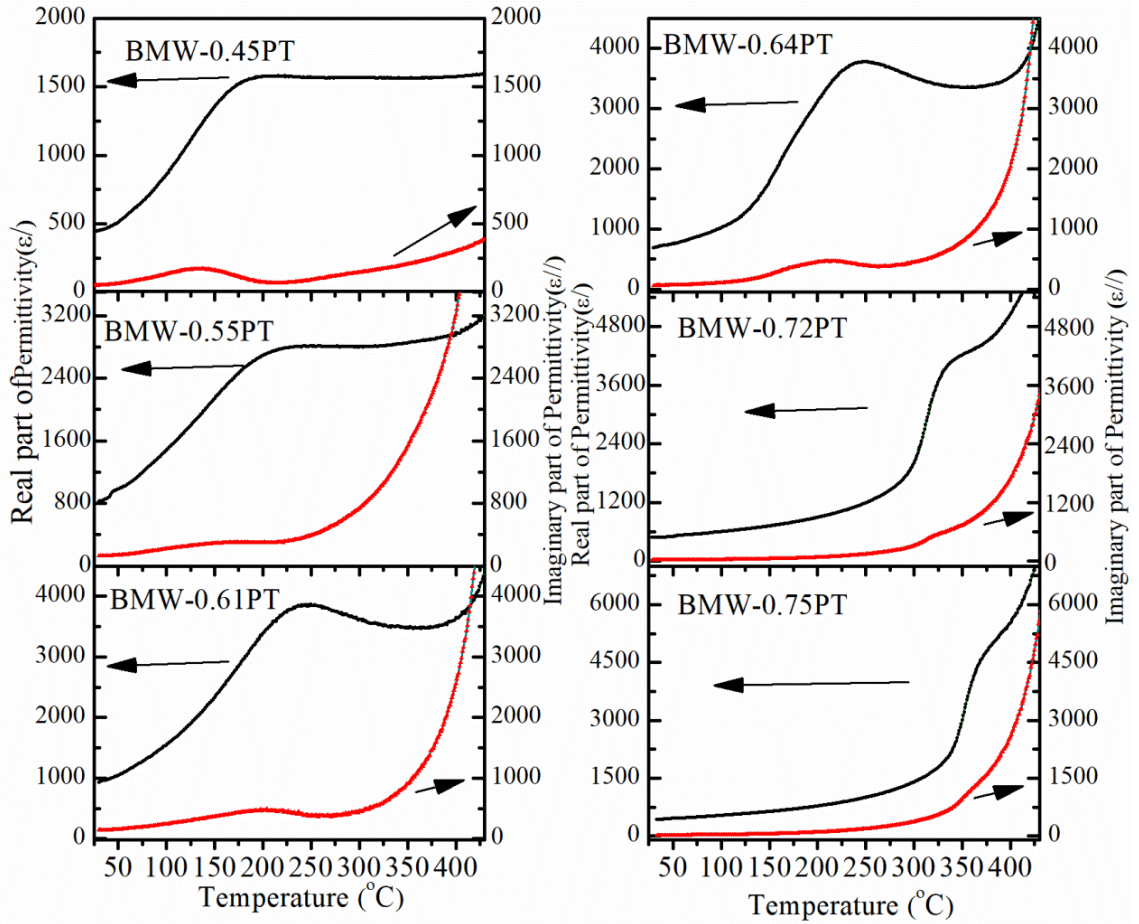
Figure 3.11 Temperatue dependence of real (ε') and imaginary (ε'') parts of the permittivity for (1-x)Bi(Mg$_{3/4}$W$_{1/4}$)O$_3$-xPbTiO$_3$ ceramics with compositions x = 0.45, 0.55, 0.61, 0.64, 0.72 and 0.75 measured at 100KHz frequency.
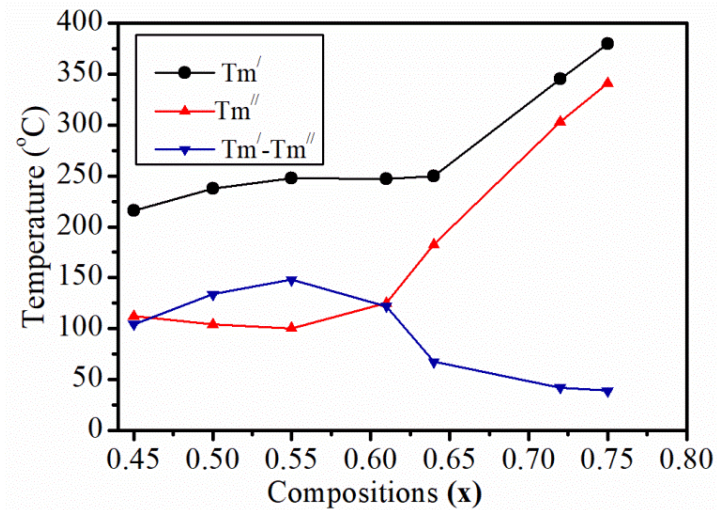
Figure 3.12 Composition dependence of the peak/anomaly temperatures in the real ($T_m^{/}$) and imaginary parts ($T_m^{//}$) of the permittivity and their difference [$T_m^{/}$-$T_m^{//}$], measured at 100 kHz for relaxor peak of $(1-x)Bi(Mg_{3/4}W_{1/4})O_3$-$xPbTiO_3$ ceramics.

3.5.5 High Temperature XRD Studies

As discussed in the previous section the temperature dependence of permittivity exhibit two peaks above room temperature and the peak on the higher temperature side appears nearly at the same temperature for all the compositions investigated. To understand the linkage of these peaks to any possible structural phase transitions, we carried out high temperature XRD studies on a composition in the phase coexistence region. **Fig. 3.13** shows the temperature evolution of selected XRD profiles for the composition with x = 0.64. The XRD data were recorded in the heating run measurements. As discussed in section 3.5.1, the room temperature structure of this composition consists of coexisting cubic (*Fm-3m*) and tetragonal (*I4/m*) phases. As can be seen from **Fig. 3.13**, with increasing temperature there is no significant change in the XRD profiles till 100°C. The intensity of the XRD peaks corresponding to the cubic phase increase drastically for the

XRD data recorded at 150°C. The intensities of the peaks of the cubic phase enhance further for the XRD data at 200°C, and it becomes the majority dominant phase. The intensities of the XRD peaks corresponding to the tetragonal phase are significantly lowered than that of the cubic phase at 200°C. For further higher temperature at 250°C, the intensities of the peaks corresponding to the tetragonal phase are very small and could be seen only as small tails of the XRD peaks for the cubic phase. The XRD profiles of the data recorded at 650°C show singlet character consistent with the cubic structure. The superlattice reflection around ~19.20° due to B-site cationic ordering is clearly seen in XRD pattern at 650°C.
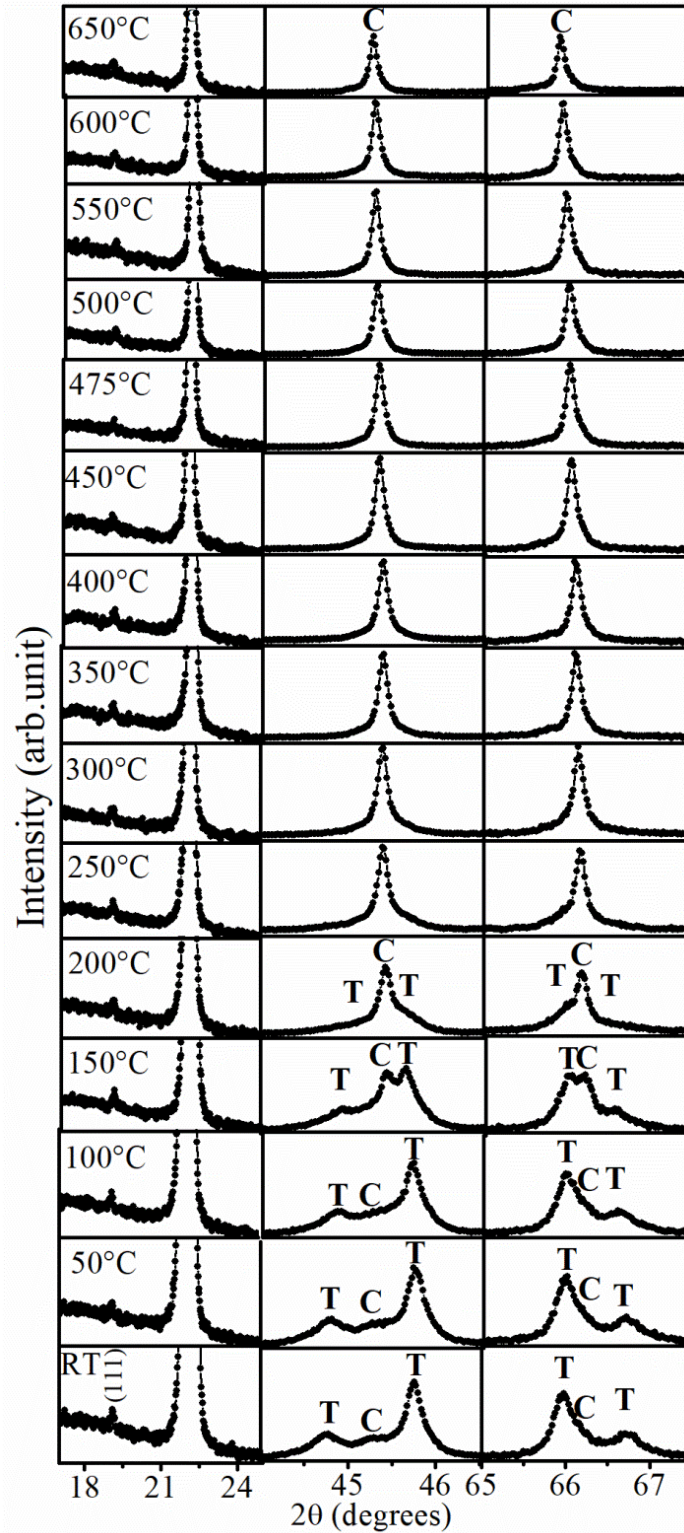
Figure 3.13 Temperature evolutions of selected XRD peak profiles of 0.36BMW-0.64PT ceramics. The peaks marked with "C" and "T" is due to the cubic and tetragonal phases.

This suggests that the high temperature structure of BMW-PT is cubic in the *Fm-3m* space group. The (400) and (440) XRD profiles for the data at 300°C and above are nearly singlet corresponding to the cubic phase which suggests that the ordered tetragonal (*I4/m*) to the ordered cubic (*Fm-3m*) phase transition is taking place below this temperature. As shown in **Fig. 3.9**(d) the temperature dependence of permittivity has a rising trend at 150°C, exhibit a peak ~250°C followed by a downward trend and then second peak ~475°C. This suggests that first permittivity peak in the temperature dependent dielectric measurement corresponds to the tetragonal (*I4/m*) to cubic (*Fm-3m*) structural phase transition. A careful examination of the (111) XRD profile corresponding to B-site ordering suggests that its intensity is slightly decreased for the XRD patterns at temperatures more than 400°C. This indicates that a part of the ordered structure is transforming into disordered cubic phase.

To investigate precisely the structural evolution of BMW-PT with temperature, we carried out Rietveld structural analysis of the diffraction data recorded at various temperatures. **Fig. 3.14** shows the Rietveld fits for the selected XRD peaks for the XRD data recorded at various temperatures using coexisting tetragonal (*I4/m*) and cubic (*Fm-3m*) phases and single phase cubic structure for the data at higher temperatures. The Rietveld fits of the XRD patterns at various temperatures is quite satisfactory. **Fig. 3.15** shows the Rietveld fits for the full pattern XRD data at 150°C (two phase region) and 650°C (cubic phase region) in the two theta range 15-100°. The overall fit is also quite good. We observed that even though the XRD profiles appear as nearly singlet for the data above 250°C, we need to consider small coexisting tetragonal (*I4/m*) phase in the Rietveld structure refinement up to the 500°C temperature. This suggests that the phase coexistence

appears in the wide temperature region and the nature of phase transition is of first order. It is further supported by the discontinuous change in the unit cell volume and lattice parameters at the phase transition temperature shown in **Fig. 3.16**.
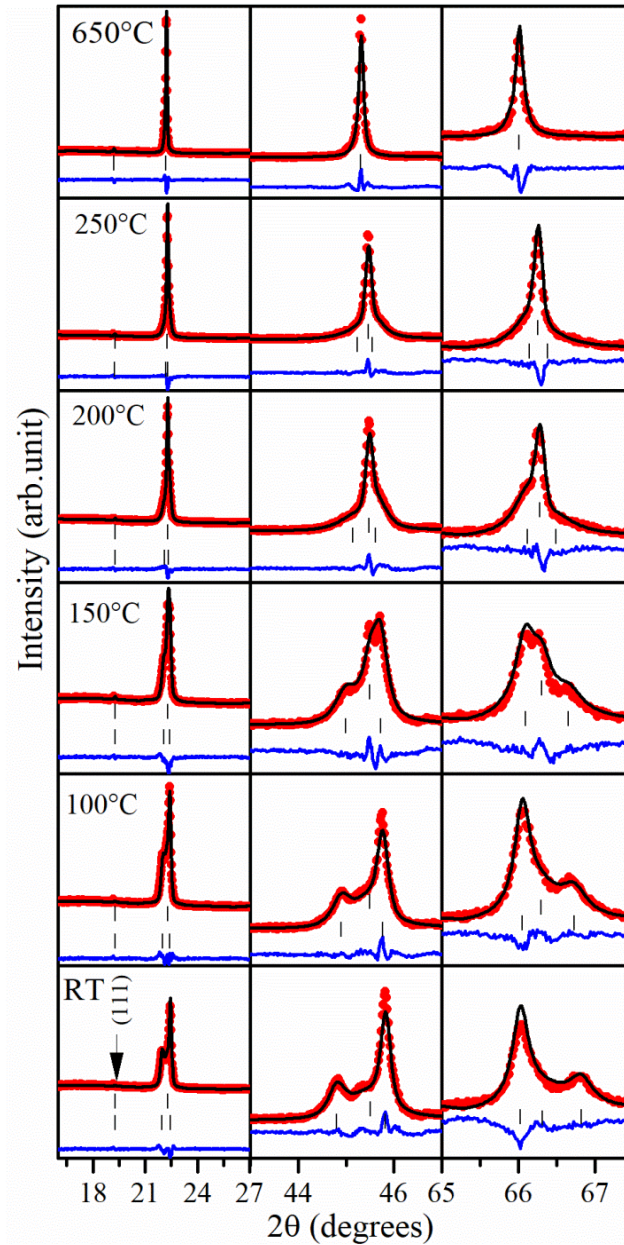

Figure 3.14 Rietveld fits for the selected XRD peaks of 0.36BMW-0.64PT ceramics using coexisting tetragonal (*I4/m*) and cubic (*Fm-3m*) phases at lower temperatures and single cubic (*Fm-3m*) phase at higher temperatures.
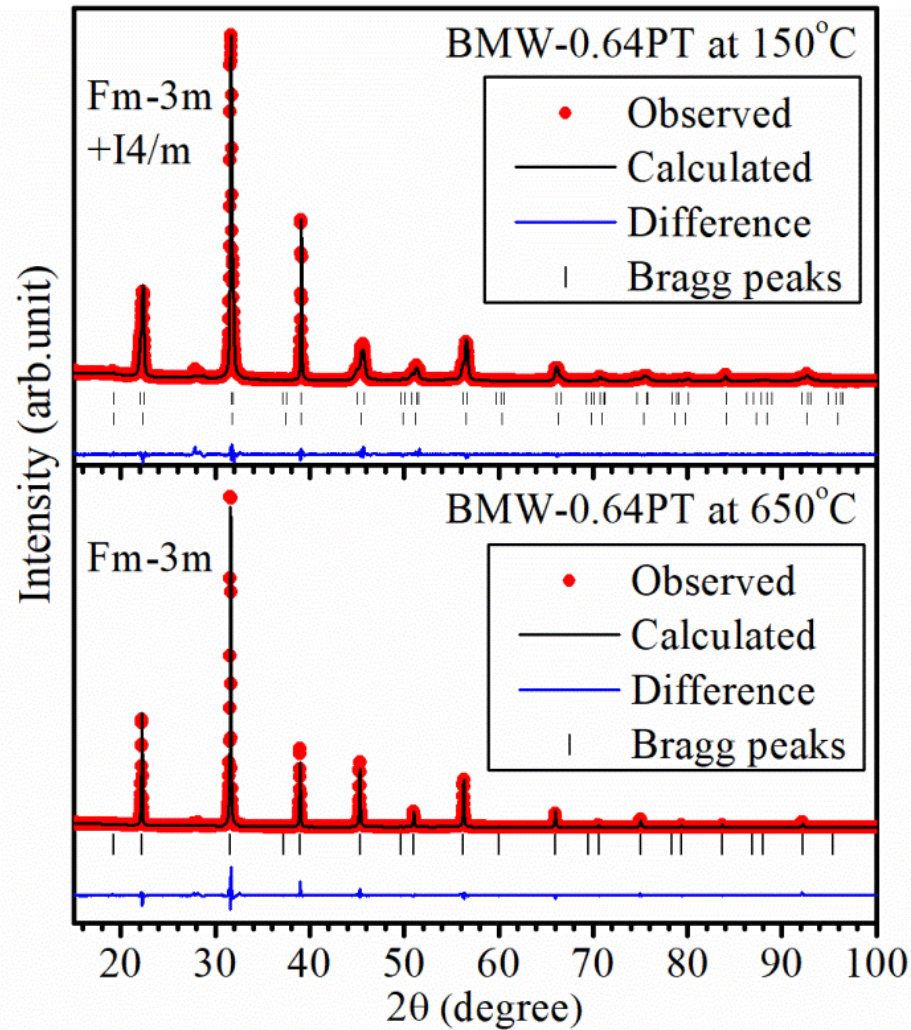
Figure 3.15 Rietveld fits for the structure of $0.36Bi(Mg_{3/4}W_{1/4})O_3\text{-}0.64PbTiO_3$ using Cubic(*Fm-3m*) + tetragonal (*I4/m*) and cubic (*Fm-3m*) structures, for the XRD pattern measured at 150°C (two phase region) and 650°C (cubic phase region), respectively.
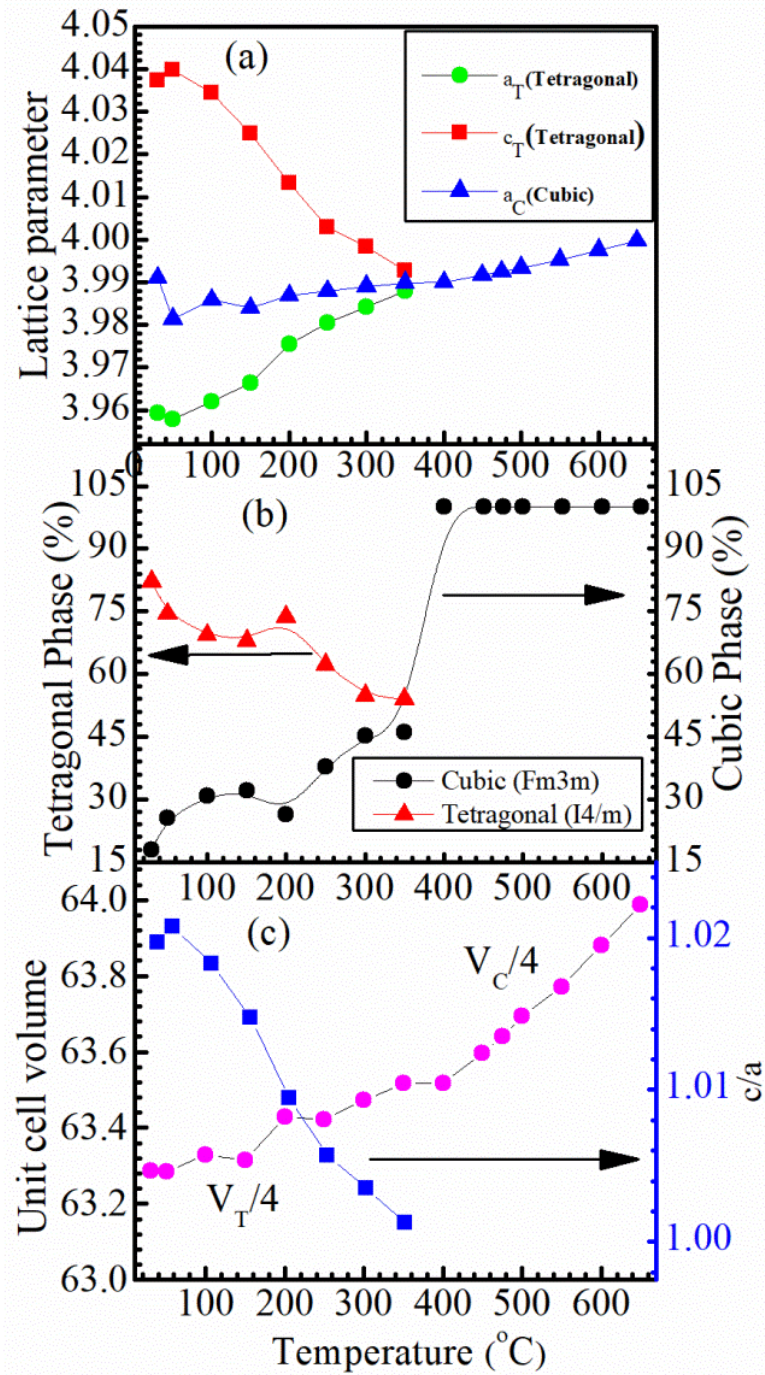
Figure 3.16 Temperature dependent (a) Lattice parameters, (b) phase fraction of cubic and tetragonal phases (c) unit cell volume and tetragonality for 0.36BMW-0.64PT ceramic.

Temperature evolution of lattice parameters, phase fraction of the cubic/tetragonal phases and, unit cell volume and tetragonality are shown in **Fig. 3.16**(a), (b) and (c), respectively. With increasing measurement temperature 'a' and 'c' parameters of the tetragonal phase come closer with the loss of tetrgaonality and merge to each other after 350°C with complete loss of the tetragonality. As shown in **Fig. 3.16**(b) the phase fraction of the tetragonal and cubic phases are unchanged till 150°C and then cubic phase fraction start increasing till the phase transition is complete with the single cubic phase above 350°C. The variation of the unit cell volume with temperature is shown in **Fig. 3.16**(c), exhibits discontinuous change around tetragonal to cubic phase transition suggesting first order nature of the phase transition.

3.5.6 New Phase Diagram of BMW-xPT Ceramics

Using the results of structural analysis, temperature dependent dielectric and XRD studies, we established a new phase diagram of (1-x)BMW-xPT ceramics as shown in **Fig. 3.17**. The dotted vertical lines demarcate the stability region of various crystallographic phases. The compositions with $x \leq 0.55$ are ordered cubic phase with space group Fm-3m. On heating above room temperature these compositions exhibit a relaxor transition which is accompanied by strong peak in the temperature dependence of permittivity. Data points shown in this region of the phase diagram correspond to the dielectric relaxational peak temperature while the high temperature crystal structure is also ordered cubic in *Fm-3m* space group. The compositions with $0.60 < x < 0.70$ exhibit coexistence of ordered cubic (*Fm-3m*) and ordered tetragonal (*I4/m*) phases at room temperature. On heating above room temperature, the ordered tetragonal phase transforms to ordered cubic (*Fm-3m*) phase. The phase boundary, corresponding to this transition shown in **Fig. 3.17**, is

determined by transition temperatures in dielectric permittivity (first peak) and also confirmed by high temperature XRD studies. The compositions with x > 0.70 are predominantly ordered tetragonal (*I4/m*) and transform to ordered cubic (*Fm-3m*) phase at higher temperatures. At higher temperatures, small fraction of disordered cubic (*Pm-3m*) phase is also expected which is not shown in the phase diagram. More studies will be needed to characterize this aspect of the phase diagram. The phase boundary between ordered tetragonal (*I4/m*) and disordered tetragonal (*P4mm*) structures for higher PT concentration compositions is also difficult to determine. The extrapolation of the composition dependence of ($\Delta T = T_m{}' - T_m{}''$) shown in **Fig. 3.12** suggests that ΔT will be zero corresponding to the composition with x = 0.85.
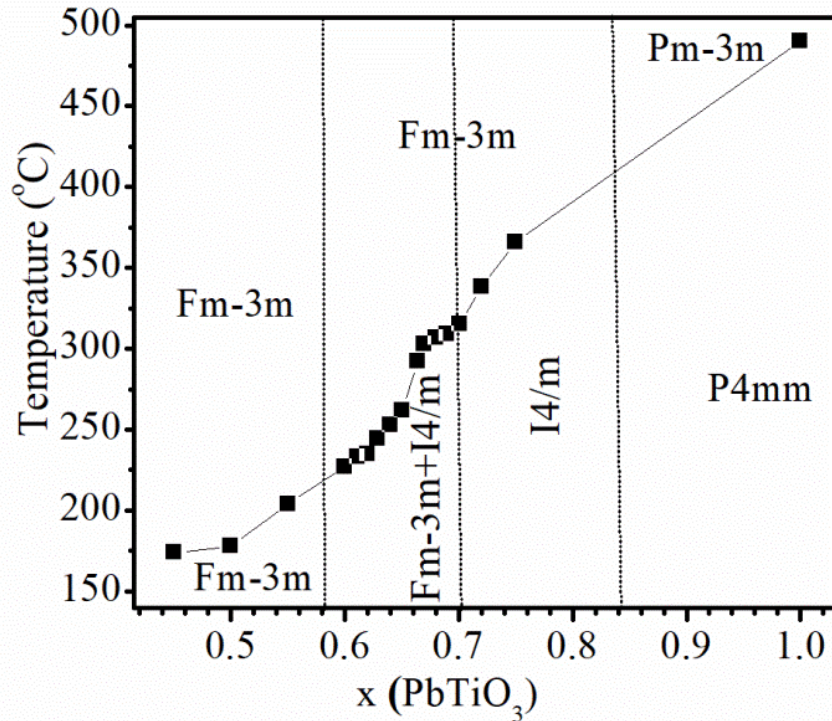

Figure 3.17 New Phase diagram of (1-x)Bi(Mg$_{3/4}$W$_{1/4}$)O$_3$-xPbTiO$_3$ ceramics.

We have shown therefore in **Fig. 3.17**, the phase boudnary between ordered tetragonal (*I4/m*) and disordered tetragonal (*P4mm*) phase at x = 0.85. The composition with x > 0.85 are expected to be disordered tetragonal phase with space group *P4mm* which will transform to disordered cubic (*Pm-3m*) phase at higher temperatures. More studies are underway to fully characterize various phase boundaries and phase transitions in BMW-PT ceramics and will be reported in future communications.

3.6. Conclusions

To summarize, the Rietveld structural and Raman spectroscopic investigation of (1-x)BMW-xPT solid solution in the composition range $0.45 \leq x \leq 1.0$ reveals the coexistence of the ordered cubic (*Fm-3m*) and ordered tetragonal (*I4/m*) structures for the composition range $0.60 \leq x \leq 0.70$ corresponding to the mrophotropic phase boundary. The compositions with $x \leq 0.55$ have ordered cubic structure in *Fm-3m* space group and the compositions with $x \geq 0.72$ have ordered tetragonal structure in *I4/m* space group which gradually transform to disordered tetragonal (*P4mm* space group) phase at higher PT concentrations. The (1-x)BMW-xPT compositions around MPB exhibit two dielectric anomalies in the temperature dependence of permittivity above room temperature. The first anomaly exhibit relaxor nature of phase transition and second anomaly is due to dielectric relaxation of defects resulting from the multiple charge states of B-site cations. On the basis of our detailed structural and temperature dependent dielectric studies we have constructed a new phase diagram of (1-x)BMW-xPT ceramics.

This chapter presents the results of structural and dielectric studies on (1-x)[Bi(Mg$_{3/4}$W$_{1/4}$)O$_3$]-xPbTiO$_3$ ceramics across the morphotropic phase boundary to investigate the crystal structure and structure-property correlations. Rietveld structure

refinement reveals that the structure of the morphotropic phase boundary compositions consists of coexisting ordered tetragonal and cubic phases, not reported earlier. The difference in the ionic radii and ionic charges of Mg^{2+} and W^{6+} leads to ordering of these ions at B-site in the ABO_3 perovskite structure of the solid solution, in a wide composition range. The structure is B-site ordered cubic phase in the space group *Fm-3m*, for the compositions with x ≤ 0.55. For the compositions with x ≥ 0.72, the structure is B-site ordered tetragonal phase in the space group *I*4/*m*, which gradually transforms into disordered tetragonal phase with space group *P*4*mm* for higher concentrations of $PbTiO_3$. Coexistence of both the ordered tetragonal and ordered cubic phases is observed for the intermediate compositions around morphotropic phase boundary in the composition range 0.55 < x < 0.72. Raman studies also confirm the B-site ordered structure for compositions close to morphotropic phase boundary. Composition dependence of room temperature dielectric constant shows a peak around x = 0.62 which mimics the behavior of ferroelectric solid solutions with the mrophotropic phase boundary. Temperature dependence of the permittivity above room temperature exhibits frequency dispersion and diffuse nature of phase transition. For all the compositions investigated, two peaks are observed in the temperature dependence of the permittivity above room temperature. The peak on the higher temperature side, which appears nearly at the same temperature for all the compositions, is attributed to the dielectric relaxation of defects resulting from the multiple charge states of B-site cations, creation of the oxygen vacancies and thereby W^{6+}/W^{5+} mixed ionization states. The permittivity peak on the lower temperatures side is due to structural transition from tetragonal (*I*4/*m*) to cubic (*Fm-3m*) phase, in compositions with ordered tetragonal structure as dominant phase. The peak on the lower temperatures

side in the temperature dependent permittivity for compositions with majority cubic phase is due to relaxor transition having dielectric relaxation with Vogel-Fulcher type freezing behavior. Using results of structural and dielectric studies, a new phase diagram of $(1-x)[Bi(Mg_{3/4}W_{1/4})O_3]$-$xPbTiO_3$ ceramics is established.